CONDENSED MATTER PHYSICS

Uniaxial spin texture in a superconducting electron gas revealed by exchange interactions

Junyi Yang[1]†, Changjiang Liu[1,2]†, Xianjing Zhou[3,4,5], Hanyu Hou[6], Kaijun Yin[6], Jianguo Wen[3], John Pearson[1,3], Alexey Suslov[4], Dafei Jin[3,7], Jidong S. Jiang[1], Ulrich Welp[1], Jian-Min Zuo[6], Michael R. Norman[1], Anand Bhattacharya[1]*

Copyright © 2026 The Authors, some rights reserved; exclusive licensee American Association for the Advancement of Science. No claim to original U.S. Government Works. Distributed under a Creative Commons Attribution License 4.0 (CC BY).

Two-dimensional (2D) superconductors with spin-textured Fermi surfaces can be a platform for realizing unconventional pairing states and are of substantial interest in the context of quantum information science and superconducting spintronics/orbitronics. We observed an unusual in-plane uniaxial anisotropy in the superconducting 2D electron gas (2DEG) formed at $EuO_x/KTaO_3$ (110) interfaces. This anisotropy is not evident in $AlO_x/KTaO_3$ (110) where the overlayer is nonmagnetic. Our results are consistent with a highly anisotropic "half-Rashba" spin-textured Fermi surface in 2DEGs formed at the $KTaO_3$ (110) interface that is hidden from external magnetic fields due to a near cancellation between orbital and spin moments but revealed by exchange interactions of the electrons in the 2DEG with Eu moments near the $EuO_x/KTaO_3$ (110) interface. The interactions between the uniaxial spin texture and the magnetic overlayer offer previously unexplored ways to explore the interplay between magnetism and 2D superconductivity.

INTRODUCTION

The interplay of large spin-orbit coupling (SOC) with crystalline symmetry breaking can result in nontrivial spin textures for electrons at the Fermi surface of a two-dimensional electron gas (2DEG) (*1*, *2*). Broken inversion symmetry along the out-of-plane direction in 2DEGs leads to a "Rashba" spin texture, where spins are locked in-plane with opposite helicity on spin-split Fermi surfaces (*3*), and such asymmetric SOC also allows for superconductivity with mixed parity (*4*, *5*). The presence of strong SOC with in-plane inversion symmetry breaking or broken orbital degeneracy can lead to an "Ising" spin texture that locks spins along the out-of-plane direction, and, for superconducting 2DEGs, this results in large in-plane critical fields (*6*–*8*) well in excess of the Pauli limit and may lead to unconventional superconductivity (*9*). These spin textures are nominally not expected to give rise to an anisotropic response to in-plane magnetic fields. Rather, such a response is often associated with effective mass anisotropy, nematicity (*10*), and superconducting order parameters with mixed-parity (*11*). On the other hand, an asymmetric strong SOC in a 2DEG with reduced symmetry can result in an anisotropic Rashba interaction, where the spins may have an in-plane anisotropy or even be locked-in along an axis for a "half-Rashba" interaction (*12*). Such a uniaxial spin texture of the Fermi surface would lead to superconductivity with inherent in-plane anisotropy, which is of both fundamental interest (*13*) and may also be relevant for applications in quantum information science (*14*), superconducting spintronics, and orbitronics (*15*, *16*).

Superconductivity was recently discovered in 2DEGs formed at interfaces of $KTaO_3$ (KTO) (*17*). Notably, the critical temperature (T_c) in KTO 2DEGs was found to strongly depend on the orientation of the interface (*17*–*19*), and it was proposed that the orientation dependence of T_c is due to varying levels of degeneracy in the t_{2g} manifold of the Ta-5d bands in quantum-confined 2DEGs formed on different crystalline facets of KTO (*19*). For the KTO (110) interface (Fig. 1A), the degenerate d_{xz}/d_{yz} states at the Γ point are lower in energy than d_{xy} due to confinement along the [110] axis, and they form an anisotropic Fermi surface with larger/smaller effective mass along the $[1\bar{1}0]$/[001] axis (*20*), respectively. Furthermore, the d_{xz}/d_{yz} states at Γ form the combination $d_{yz} \pm id_{xz}$ with an orbital angular momentum axis oriented along the in-plane [001] direction. Due to SOC, the spins antialign to these orbital moments, and this gives rise to an in-plane anisotropy for both orbital and spin textures along [001] with no spin canting along the out-of-plane direction. Additionally, broken inversion symmetry at the KTO (110) interface gives rise to Rashba splitting of bands formed from these states, which, along with the uniaxial anisotropy, induces a dominant $\mathbf{k}_y\hat{\sigma}_x$ half-Rashba texture due to spin-momentum locking (here, x refers to [001] and y to $[1\bar{1}0]$) (Fig. 1B). We note that this uniaxial anisotropy is unique to the KTO (110) interface (*21*, *22*) and distinct from the more isotropic spin textures calculated for KTO (111) (*23*) and KTO (001) (*24*) interfacial 2DEGs. Last, as is well-known, for single-electron occupancy in the t_{2g} manifold, the orbital and spin moments are "antialigned," which leads to a strongly reduced g-factor (*25*), and a reduced Zeeman coupling of external magnetic fields (*26*) to the electronic spin texture. Thus, KTO interfacial 2DEGs are nominally expected to have a relatively weak response to in-plane magnetic fields.

RESULTS

In this work, we report on a uniaxial in-plane spin texture for KTO_3 (110) interfaces, which is revealed by the anisotropy of the in-plane upper critical field H_c as well as the normal state magnetoresistance for EuO_x/KTO (110) 2DEGs, where the EuO_x overlayer is magnetic. We fabricated Hall bar devices on both AlO_x/KTO (110) and EuO_x/KTO (110) (fig. S1) 2DEGs. Here, AlO_x is nonmagnetic, while EuO_x is ferromagnetic with T_{Curie} of ~70 K. Figure 1C shows the temperature

[1]Materials Science Division, Argonne National Laboratory, Lemont, IL, USA. [2]Department of Physics, University at Buffalo, SUNY, Buffalo, NY, USA. [3]Center for Nanoscale Materials, Argonne National Laboratory, Lemont, IL, USA. [4]National High Field Magnetic Laboratory, Tallahassee, FL, USA. [5]Florida State University, Tallahassee, FL, USA. [6]Department of Material Science and Engineering, University of Illinois at Urbana-Champaign, Urbana, IL, USA. [7]University of Notre Dame, Notre Dame, IN, USA.
*Corresponding author. Email: anand@anl.gov
†These authors contributed equally to this work.

Downloaded from https://www.science.org at Florida State University on September 02, 2026

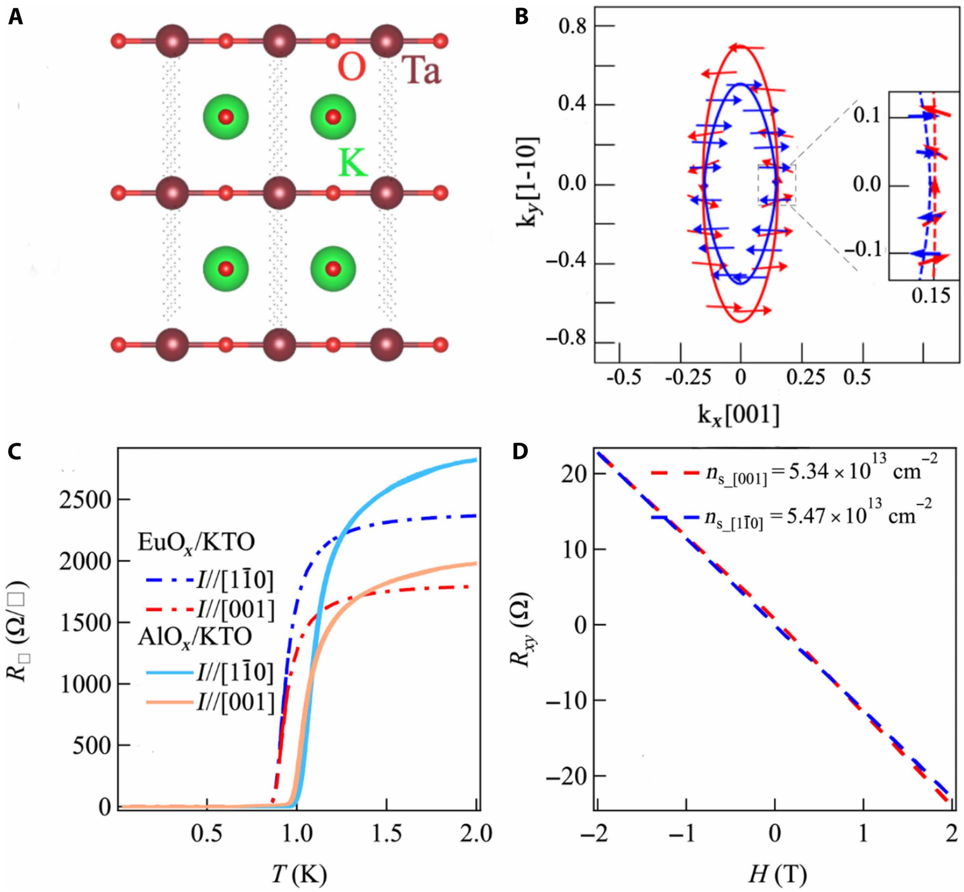

Fig. 1. Uniaxial spin texture for KTO (110) interface. (**A**) Schematic diagram of KTO (110). (**B**) KTO (110) Fermi surface derived from d_{xz}/d_{yz} states, with its anisotropic spin texture. The length of the arrows is related to the spin vector size, with the inset showing an expanded view around [001]. The two Rashba spin-split surfaces are shown in red and blue, assuming an exaggerated spin-splitting $t_R = 20$ meV to better illustrate the spin textures on the inner and outer Fermi surfaces. We assume $t_R = 2$ meV in all other calculations. (**C**) Temperature dependence of the sheet resistance of EuO_x/KTO and AlO_x/KTO with current applied along two different in-plane directions. The light blue solid line denotes the current along [1$\bar{1}$0], and the light red solid line denotes the current along [001] for AlO_x/KTO. The blue dashed line denotes the current along [1$\bar{1}$0], and the red dashed line denotes the current along [001] for EuO_x/KTO. (**D**) Hall measurements for Hall bar devices along the [001]/[1$\bar{1}$0] directions, respectively. The carrier density along both orientations is very close.

dependence of the sheet resistance ($R_\square$) for EuO_x/KTO with current along [001]/[1$\bar{1}$0], respectively. The crystallographic axis for each direction is determined through x-ray diffraction (fig. S2). Superconductivity is observed for both samples below 800 mK. The normal state $R_\square$ for a current along [1$\bar{1}$0] is found to be larger than that for a current along [001] by a factor of 1.5 for all samples. These observations are consistent with a highly anisotropic Fermi surface of KTO (110) (Fig. 1B) (*20*), where the effective mass along the [1$\bar{1}$0] direction is larger than that along [001]. Hall measurements (Fig. 1D) along these two crystallographic directions are nearly identical, and, presumably, the anisotropic $R_\square$ is due to the anisotropy in electron mobility. We note that, for LAO/STO (110), a similar anisotropy in $R_\square$ is observed, although it changes as a function of carrier density (*27–29*) due to occupation of the d_{xy} bands at higher densities. In contrast, for our KTO (110) 2DEGs, the anisotropy of the normal state $R_\square$ is found to be similar for both low and high densities. This may imply that the d_{xy} bands are not occupied or have fewer carriers than the d_{xz}/d_{yz} band in our KTO (110) 2DEGs, presumably due to the stronger confinement effects in KTO (110) relative to STO (110). However, we note that recent angle-resolved photoemission experiments on doped KTO (110) surfaces with higher carrier density (~7×10^{13}/cm^2) do observe the occupation of the higher lying d_{xy} bands (*20*).

Anisotropic superconductor-ferromagnet interaction in EuO_x/KTO (110) near T_c

To explore the anisotropic spin texture in KTO (110), we first measured the in-plane magnetic field dependence of $R_\square$ for EuO_x/KTO (110). We find evidence for coupling between conduction electrons in the 2DEGs and the magnetic EuO_x overlayer in measurements of $R_\square$(H) at 2 K (above T_c), where we observe hysteretic behavior at low fields for H//[001] (Fig. 2A). Notably, the magnetoresistance (MR) = $\frac{R(H)-R(0)}{R(0)}$ and the apparent hysteresis for H//[001] is much larger than that for H//[1$\bar{1}$0]. The hysteretic minima in $R_\square(H)$ at ±115 Oe are consistent with the in-plane coercive field of the EuO_x overlayer of ~115 Oe from magnetization measurements on this sample. The magnetization-versus-H measurements of the EuO_x

Downloaded from https://www.science.org at Florida State University on September 02, 2026

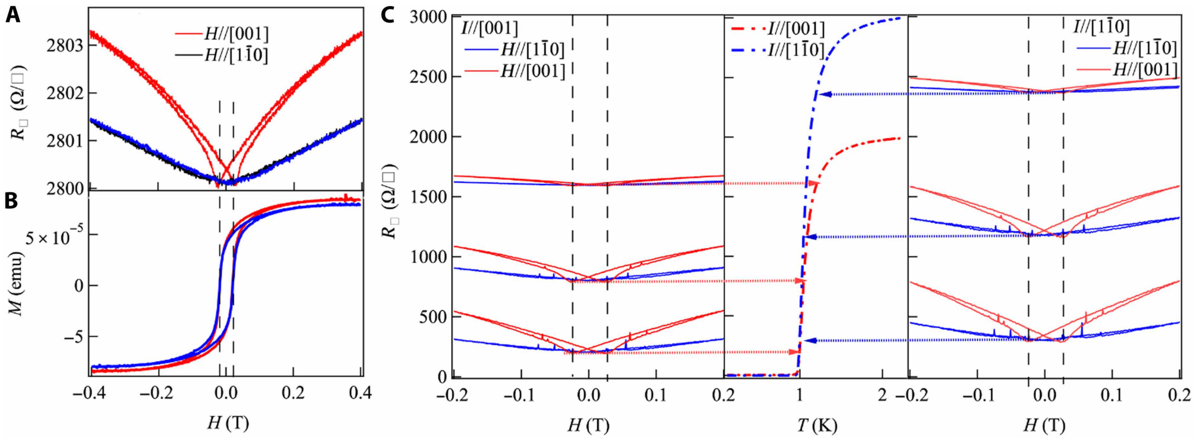

Fig. 2. Anisotropic magnetoresistance in EuO/KTO (110). (**A**) Field dependence of the sheet resistance for EuO/KTO (110) at 2 K. The red solid line denotes a field along [001], and the blue solid line denotes a field along [1$\bar{1}$0]. (**B**) Field dependence of the magnetic moment for EuO/KTO (110) at 2 K, showing a nearly isotropic coercivity. The red solid line denotes a field along [001] and the blue solid line denotes a field along [1$\bar{1}$0]. (**C**) Field dependence of the sheet resistance for EuO/KTO (110) with current applied along different crystal axes. The left panel shows the field dependence of the sheet resistance when the current is applied along [001]. The right panel shows the field dependence of the sheet resistance when the current is applied along [1$\bar{1}$0]. The red solid line denotes a field along [001], and the blue solid line denotes a field along [1$\bar{1}$0]. The central panel shows the temperature dependence of the sheet resistance for *I*//[001] (red solid dashed line) and *I*//[1$\bar{1}$0] (blue solid dashed line). The arrows are used to indicate the different temperatures that the field dependence of the resistance is measured.

Downloaded from https://www.science.org at Florida State University on September 02, 2026

overlayer are nearly identical for H//[001] and H//[1$\bar{1}$0], implying that the observed MR anisotropy is inherent to the KTO 2DEG and not the magnetization of the EuO_x overlayer. As the temperature is lowered toward T_c, the MR rapidly increases in magnitude, approaching ~130% for H//[001], and ~47% for H//[1$\bar{1}$0] for $H = 0.2$ T at a temperature of ~1 K. We also find that the highly anisotropic MR is independent of the current direction, from our measurements on Hall bars oriented along [001] and [1$\bar{1}$0] on the same sample, indicating that the anisotropy in the MR only depends on the orientation of the magnetic field with respect to the crystal lattice. We also note a weak anomaly in the temperature dependence of the MR near the Curie temperature of the EuO_x overlayer (fig. S3), further evidence for its coupling to electrons in the KTO 2DEG.

We note that a hysteretic MR has been observed in 2DEGs formed at $LaAlO_3/SrTiO_3$, $GdTiO_3/SrTiO_3$, and $LaTiO_3/SrTiO_3$ interfaces when magnetism is induced (*30*–*32*), and recent work also shows hysteretic MR at KTO interfaces (*33*, *34*). However, the in-plane anisotropy in MR that we observe has not been reported earlier to the best of our knowledge. The anisotropy of the MR near the superconducting transition in Fig. 2 is consistent with a pair-breaking effect that arises from interfacial exchange coupling of ferromagnetic Eu spins in EuO_x with the highly anisotropic in-plane uniaxial spin texture of KTO (110) 2DEGs. However, this low-field MR for in-plane fields, including the hysteretic behavior, is no longer observed once we cool below T_c as the experimentally measured in-plane H_c increases far above the coercivity field of the EuO_x overlayer. This also implies that the interfacial exchange coupling between the EuO_x and the KTO (110) 2DEG is relatively weak, being effective only in the transition region near T_c where the conductivity is enhanced by superconducting fluctuations, but not below T_c where the superconductivity is more robust.

Anisotropic in-plane upper critical field

We also observe a striking anisotropy in the in-plane H_c of EuO_x/KTO (110) 2DEGs as we cool below T_c. Figure 3 (A and B) shows the temperature dependence of $R_\square$ when the field is applied along the [001] and [1$\bar{1}$0] directions. Figure 3C summarizes the T dependence of H_c for both directions. T_c is taken as the inflection point in the temperature dependence of $R_\square$, normalized to its zero-field value. H_c is normalized to the conventional Pauli paramagnetic field $\mu_0 H_P [\mathrm{T}] = 1.86\ T_c\ [\mathrm{K}]$ (*35*). Note that the actual paramagnetic limiting field can be substantially higher both due to spin-orbit scattering and a reduced g-factor (*36*, *37*). At the lowest temperatures, in EuO_x/KTO (110), we find that H_c//[1$\bar{1}$0] < H_c//[001] where $\frac{H_c//[1\bar{1}0]}{H_c//[001]} \sim 0.8$ (Fig. 3 and fig. S9D). However, closer to T_c, this ratio strongly inverts and $\frac{H_c//[1\bar{1}0]}{H_c//[001]} > 7$at $T = 0.9\ T_c$. This switching of anisotropy in H_c is observed in several EuO_x/KTO (110) samples, for a range of T_c values (figs. S5 to S7). The twofold nature of the anisotropy in H_c close to T_c is evident in the angular dependence of the normalized $R_\square$, $R_{ANI}(\varphi) = R_\square(\varphi)/R_\square(\varphi = 0)$ (here, $\varphi = 0$ for H//[001]), in a 0.5 T in-plane magnetic field (Fig. 3D). A dumbbell-shaped $R_{ANI}(\varphi)$ is observed with minima for magnetic fields along [1$\bar{1}$0], implying H_c//[1$\bar{1}$0] > H_c//[001].

In addition, we also measured the dependence of T_c on in-plane magnetic fields along [001] and [1$\bar{1}$0] for AlO_x/KTO (110) samples (fig. S8). Figure 3E summarizes the T dependence of H_c for the [001] and [1$\bar{1}$0] directions for AlO_x/KTO (110) with $T_c = 1080$ mK. In contrast to EuO_x/KTO (110), for AlO_x/KTO(110), the ratio of upper critical fields $\frac{H_c//[1\bar{1}0]}{H_c//[001]} \sim 0.98$ near T_c and reduces monotonically to ~0.8 at the lowest temperatures, with no inversion. The same anisotropy is found in a lower T_c sample (fig. S9). We also measure $R_{ANI}(\varphi)$ in a 0.5-T in-plane (Fig. 3F) for a fixed current direction to obtain the full angular dependence of MR at $T \lesssim T_c$ for AlO_x/KTO, and we find it to be nearly isotropic.

The H_c-versus-T-phase diagrams for EuO_x/KTO (110) and AlO_x/KTO (110) are very different. Despite the highly anisotropic spin-texture anticipated for KTO (110) 2DEGs, the anisotropy observed in AlO_x/KTO (110) can be explained entirely by the anisotropy of the orbital-limiting field. A square-root–like H_c-versus-T variation

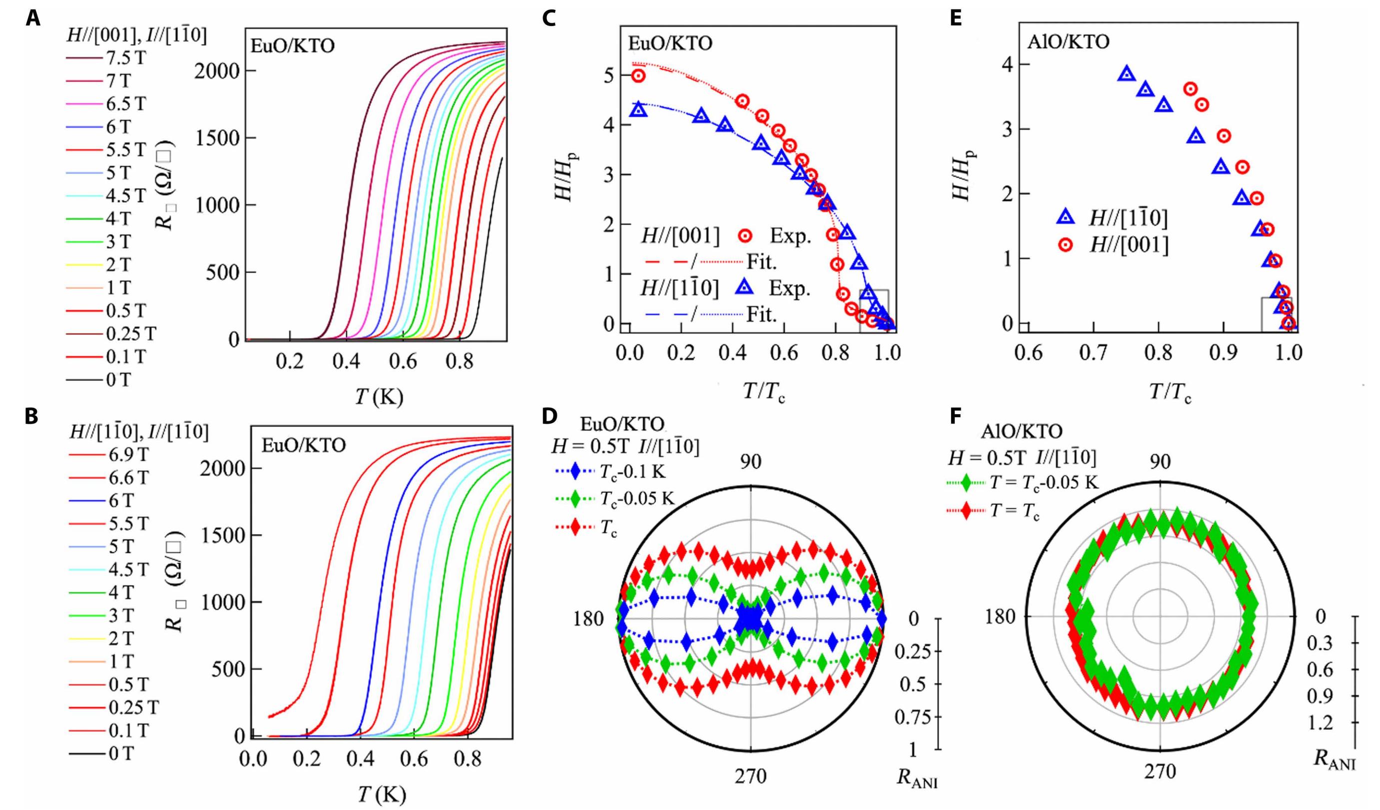

Fig. 3. Anisotropic critical field for KTO (110). Temperature dependence of the sheet resistance of EuO_x/KTO for different in-plane fields when (**A**) the field is applied along [001] and (**B**) when the field is applied along [1$\bar{1}$0]. (**C**) Temperature dependence of the critical field of EuO_x/KTO for the [1$\bar{1}$0] and [001] field directions. T_c is normalized to its zero-field value, and H_c is normalized to the Pauli paramagnetic field. The solid/dashed line denotes fits based on the KLB/WHH models described in the text. (**D**) The angular dependence of the normalized sheet resistance of EuO_x/KTO for an in-plane field of 0.5 T for three different temperatures. A lower R_{ANI} would imply a higher value of H_c. (**E**) Temperature dependence of the critical field of AlO_x/KTO for the [1$\bar{1}$0] and [001] field directions. (**F**) The angular dependence with respect to the field direction of the normalized sheet resistance for AlO_x/KTO with a field of 0.5 T at two different temperatures. A higher R_{ANI} would imply a lower value of H_c.

for AlO_x/KTO (110) is consistent with Ginzburg-Landau theory for a single band two-dimensional (2D) superconductor with an anisotropic mass tensor (*38*), where the ratio of the orbital critical field along the two in-plane directions is approximately related to the inverse ratio of the effective masses. Our resistance measurements in the normal state are consistent with an effective mass $m_{[1-10]} > m_{[001]}$, resulting in H_c//[001] > H_c//[1$\bar{1}$0], as observed. Fits of the critical field using Werthamer-Helfand-Hohenberg (WHH) (*39*) theory for a lower T_c sample with a wider dynamic range in temperature are consistent with a reduced *g*-factor (fig. S16). While effective mass anisotropy is temperature independent, a reduced *g*-factor combined with anisotropic spin-orbit scattering can result in a modest variation of the anisotropy as a function of temperature (fig. S16).

On the other hand, the unconventional H_c-versus-T data for EuO_x/KTO suggest contributions of both orbital and spin pair-breaking effects. As noted earlier, at temperatures below T_c, we do not observe hysteretic effects at fields of ~115 Oe as we did for the data in Fig. 2. Furthermore, the ferromagnetic EuO_x moment saturates well below the fields where we continue to observe a strong reduction in H_c versus T (the "crossing point" is at $H > 3$ T, while the EuO_x moment saturates at $H < 0.4$ T). Thus, we believe that the observed effects for $T < T_c$ are not due to ferromagnetic EuO_x. Rather, our data are reminiscent of Chevrel phase superconductors like $EuMo_6S_6$ where an internal field due to the presence of local moments has a profound impact on H_c and can give rise to an inflection-like behavior near T_c (*40*). We suggest a scenario involving paramagnetic Eu^{2+} impurity ions that diffuse into KTO (*17*, *41*, *42*) and interact via exchange interactions with the anisotropic spin texture of the KTO (110) 2DEG. The external field rapidly polarizes the Eu^{2+} spins at low temperatures, and they, in turn, interact with electrons at the Fermi surface via said exchange interaction. This gives rise to an extra pair-breaking term that acts to suppress H_c for temperatures near T_c, which follows the polarization of the Eu moments. While an exchange coupling also exists between the ferromagnetic Eu^{2+} in EuO_x and conduction electrons in 2DEGs, the ferromagnetic moment rapidly saturates below 0.1 T; thus, it is insufficient to support the continued rapid change of critical field in EuO_x/KTO (110) for fields beyond 1 T applied along [001] near T_c. We note that the external magnetic fields interact via the Zeeman effect with the total moment ($L + 2S$) of the electrons in the KTO (110) 2DEGs, which is strongly reduced due to the antialigned orbital and spin moments that nominally cancel. On the other hand, the exchange interaction between the Eu^{2+} impurities and the conduction electron in the KTO (110) 2DEG involves only the electron spin (S) and is not affected by the reduced total moment.

Downloaded from https://www.science.org at Florida State University on September 02, 2026

To illustrate this, we generalize an approximate formula given by Klemm, Luther, and Beasley (KLB) (*43*) by including an exchange field in their pair-breaking function $\alpha(h)$ that determines H_c

$$\ln(t) = \psi\left(\frac{1}{2}\right) - \psi\left[\frac{1}{2} + \frac{\alpha(h)}{2\pi k_B T}\right] \quad (1)$$

where ψ is the digamma function, t is the reduced temperature (T/T_c), and h is the reduced field, which enters $\alpha(h)$as h^2 as we are considering in-plane fields.

$$\alpha(h) = ch^2 + \frac{1}{2b}\left[\left(\frac{g}{2}\right)h + h_J\right]^2 \quad (2)$$

where c is πT_c, b^{-1} is $3\tau_{so}$ with τ_{so} being the spin-orbit scattering time, and h_J is the reduced exchange field between the paramagnetic Eu^{2+} impurity ions ($J = 7/2$) and the tantalum conduction electrons, which is described by a Brillouin function $h_J = h_{J0} B_J\left(Jg' \mu_B H / k_B T\right)^{30}$ ($g' = 2$). The first term in $\alpha(h)$ contributes to orbital pair breaking, while the second term includes contributions from the Zeeman and exchange coupling to the spins of the conduction electrons. Here, h_{J0} is the magnitude of the exchange field depending on the microscopic exchange integrals and the concentration of Eu-ions. h_{J0} also depends on the angle between the in-plane field h and the [001] axis due to the anisotropy of the spin texture of the Ta-5d states. Because the spin texture in Fig. 1B has a uniaxial in-plane anisotropy, h_J is larger for fields along [001] compared to fields along [1$\bar{1}$0]. Thus, when the external field is applied along the [001] direction, the pair-breaking function $\alpha(h)$ will rapidly increase at small fields following the H/T dependence of the Brillouin function. Due to this “boost” to $\alpha(h)$ provided by the exchange field, the required external field for pair-breaking is greatly reduced, and H_c//[001] is much smaller for T near T_c. Once the moment is saturated, the relative contribution of the “exchange” term is diminished as the field increases further. Therefore, with the decrease of temperature and, correspondingly, the increase in critical field, H_c versus T_c is gradually dominated by pair-breaking due to orbital effects. For this reason, both EuO_x/KTO and AlO_x/KTO show similar behavior at low T. We extract $\alpha(h)$ from our experimental H_c and fit it using Eq. 2 assuming $g = 0.5$ (fig. S17) and find that $\frac{h_J\,[001]}{h_J\,[1\bar{1}0]} \sim 1.33$. An alternative fit to the data can be done by using an in-plane formula for H_c, which is based on WHH supplemented by the exchange field (fig. S17) (*44*). As with the KLB fit, the exchange field has a negative sign with respect to applied field in the WHH fit, and a similar ratio of $\frac{h_J\,[001]}{h_J\,[1\bar{1}0]} \sim 1.29$ is obtained. While a nonzero g-factor implies a Zeeman contribution to pair-breaking from the applied field, the exchange field remains the dominant pair-breaking factor near T_c.

Diffusion of Eu ions across the KTO (110) interface

Scanning transmission electron microscopy measurements yield information on the distribution of Eu ions in the vicinity of the EuO_x/KTO (110) interface, where cation interdiffusion and presence of O vacancies can lead to the formation of a 2D electron gas (*42*). Figure 4A shows a cross-sectional high-angle annular dark field (HAADF) image along the KTO [110] zone-axis orientation, where the Eu ions that have diffused into KTO are evident from the enhanced Z-contrast on the K sites (Fig. 4B and fig. S11), up to several atomic layers into the KTO. To obtain further insight regarding diffusion of Eu, we also analyze the interfacial composition using energy-dispersive x-ray spectroscopy (EDS) (Fig. 4C). The concentration of Eu decreases as it goes from EuO_x into KTO, and the presence of Eu persists beyond 5 nm into KTO (Fig. 4D). Electron energy loss spectroscopy (EELS) of Eu also indicates diffusion of Eu into the KTO (Fig. 4E). In particular, the Eu fine structure measured using EELS reveals new satellite peaks that emerge when scanning from EuO_x into the KTO (Fig. 4E). The intensity of the satellite peak at 1133 eV corresponding to Eu^{3+} rises near the interface before decaying in the KTO within 6.8 ± 1.0 nm, while the spectral signatures for Eu^{2+} peaked at 1135.2 eV decay smoothly going from EuO_x into the KTO within about 3.7 ± 1.1 nm. This is within the effective thickness of the superconducting electron gas at the EuO_x/KTO interface of ~7 nm (fig. S12). Thus, our findings are consistent with a mixture of Eu^{2+} and Eu^{3+} ions within KTO near the interface (Fig. 4F). The presence of Eu^{2+}, which has a magnetic moment of $7\mu_B$, is consistent with the field dependence of the pair-breaking parameter that we observe at temperatures just below T_c. On the other hand, Eu^{3+} has zero net moment and will not respond to external fields. Thus, we hypothesize that, when an external field is applied, paramagnetic Eu^{2+} ions within the KTO align with the field and interact with the electrons in the KTO (110) 2DEG through exchange coupling. Thus, we surmise that diffusion of Eu^{2+} into KTO is central to the exchange-induced effects that we describe here, and controlling this is subject of future work.

Anisotropic WAL for in-plane magnetic fields

To further corroborate the uniaxial in-plane spin texture, we measure magnetoconductance at $T > T_c$ for in-plane fields up to 5 T, where we find signatures of an anisotropic in-plane weak antilocalization (WAL) in EuO_x/KTO (110) samples. Quantum interference of conduction electrons in the presence of SOC results in a positive magnetoresistance known as WAL. WAL for an out-of-plane field has been observed for 2DEGs in both KTO (111) and KTO (110) (*36*, *45*–*47*). However, in 2DEGs formed at the $NdTiO_3/SrTiO_3$ interface, it was shown that exchange coupling due to local magnetic moments can enhance the dephasing of electrons under in-plane fields (*48*) and that WAL effects in this geometry can probe the in-plane spin susceptibility. Thus, we first measured the magnetoconductance in AlO_x/KTO (110) at different temperatures for in-plane fields along [1$\bar{1}$0] and [001] (Fig. 5, A and B). A broad quadratic field dependence of the magnetoconductance is observed along both directions, which is presumably due to Zeeman dephasing in applied in-plane fields. We observe a decrease in the magnetoconductance as the temperature increases due to the loss of phase coherence. A cusp-like behavior is only observed for fields along the out-of-plane direction (fig. S13A). This mirrors what occurs for H_c, where the orbital field enters linear in H for perpendicular fields but quadratic in H for parallel fields, given that the Cooperon that is associated with WAL has similar properties to the Cooper pair propagator for superconductivity.

Figure 5 (D and E) shows the magnetoconductance measured on EuO_x/KTO (110) at different temperatures for the two in-plane field directions. In strong contrast to AlO_x/KTO (110), a sharp cusp in the field dependence of the magnetoconductance is observed when the field is applied along [001]. As the temperature increases from 2 K, the cusp feature is attenuated, and the magnetoconductance decreases sharply as quantum corrections are lost. For fields applied along [1$\bar{1}$0], a noticeably broader cusp-like feature is observed at 2 K, but with a similar temperature dependence as for [001]. Because the orbital corrections to the magnetoconductance should be quadratic and small for in-plane fields in a quasi-2D limit, we look to the Zeeman contribution for the dephasing of WAL in the magnetoconductance (*48*)

Downloaded from https://www.science.org at Florida State University on September 02, 2026

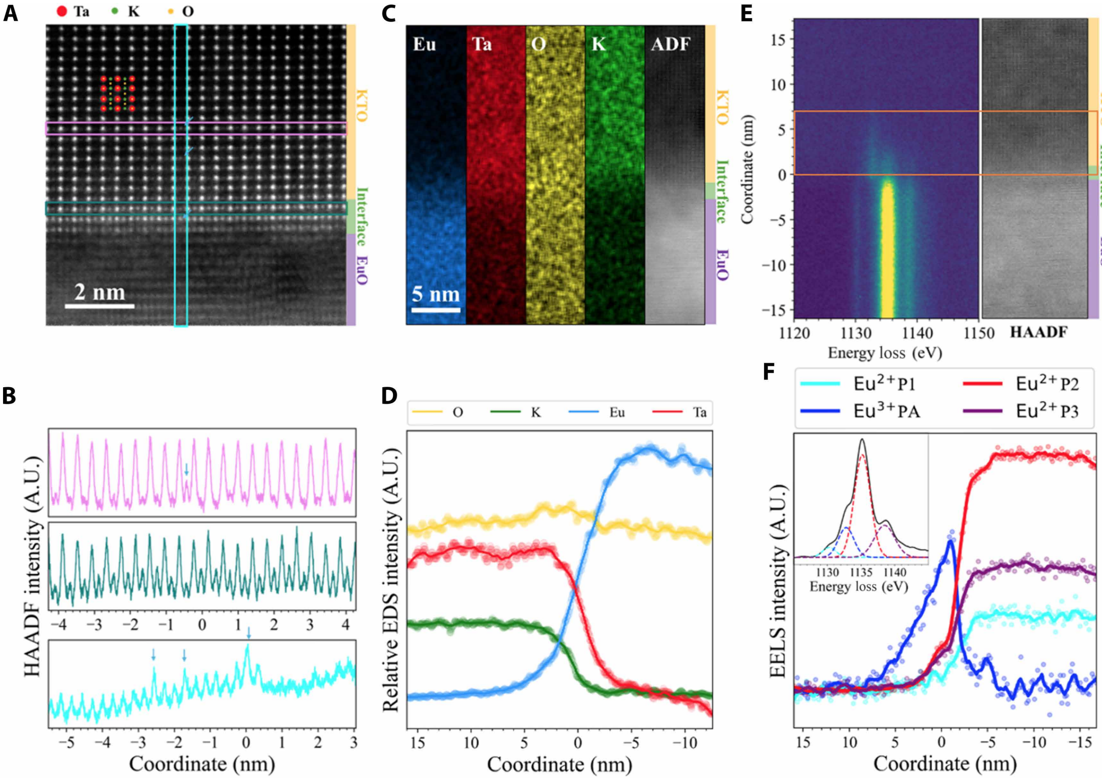

Fig. 4. Cross section of EuO/KTO(110) interface. (**A**) Atomic resolution HAADF image of a EuO/KTO [110] interface. (**B**) Intensity line profile of the three colored lines marked in (A); the higher intensity column of atoms marks the replacement of K by Eu. (**C**) Larger field-of-view energy-dispersive x-ray spectroscopy (EDS) mapping and HAADF image across the interface. (**D**) EDS intensity profile of K, Ta, O, and Eu with respect to the vertical direction in (C) from KTO to EuO across the interface. (**E**) 2D electron energy loss spectroscopy (EELS) spectra (left) correlated to the HAADF image (right) at the EuO/KTO [110] interface. The orange box indicates the spatial extent of superconductivity, overlapping with diffused Eu^{2+}/Eu^{3+} (**F**) Spatial profiles for the Eu^{2+} (1130.3, 1135.2, and 1138.5 eV) and Eu^{3+} (1132.8 eV) peaks in the EELS spectra measured across the EuO/KTO [110] interface. A selected spectrum and its decomposed peaks are shown in the inset. The zero position in (B), (D), and (F) is the EuO/KTO [110] interface. A.U., arbitrary units.

$$\Delta G(H_{//}) = -\frac{G_0}{2}\ln\left[1+\frac{\Delta_\Phi(H_{//})}{B_\Phi}\right] \quad (3)$$

where $\Delta_\Phi(H_{//}) = \frac{[2\mu_B(H_{//})]^2}{(4eD)^2 B_{so}}$. Here, D is the diffusion constant, B_{so} is the field scale associated with spin-orbit scattering, B_Φ is the orbital dephasing field scale, and G_0 is the quantum of conductance. For an in-plane field H, this gives rise to a quadratic field dependence. However, as with H_c, for EuO_x/KTO, we expect that the Eu impurity moments in the KTO 2DEGs will induce an additional exchange term that will sharply enhance the effective field that enters into the Zeeman term (*49*) $H_{//} = \frac{g}{2}H + H_J$. The first term in $H_{//}$ is small because g is strongly reduced because of quenching of the total moment, and the field-induced dephasing is dominated by the exchange interaction between Eu moments and the uniaxial half-Rashba spin-polarized electrons (Fig. 5C and fig. S13B). At low temperatures, the Eu moments align rapidly with H, leading to the pronounced boost in the exchange interaction at low fields with electrons in the KTO 2DEGs, and a quasilinear behavior is seen in the magnetoconductance. At higher fields, the impurity moments saturate, and we anticipate crossing over to a quadratic behavior as expected from orbital contributions. We thus fit our data using Eq. 3 with the same g and the same exchange field as in our H_c analysis (see table S2). These fits are excellent, indicating that our H_c and magnetoconductance analysis is consistent with one another.

DISCUSSION

For context, the crossover in the anisotropy in H_c has been observed (*50*–*52*) in a quasi-1D superconductor $K_2Cr_3As_3$, which arises from an anisotropic spin susceptibility along and perpendicular to its 1D chains, although these data do not show the pronounced inflection in H_c (T_c) we see for fields along [001] in EuO_x/KTO (110). Notably, measurements of the Knight shift in $K_2Cr_3As_3$ in the superconducting state suggest a triplet component (*53*). Twofold modulations of the in-plane H_c have also been observed in several 2D superconductors and have been attributed to emergent nematicity (*54*) and mixing of s-wave with d-wave or p-wave order parameters (*11*, *36*). While a Lorentz force resulting from magnetic fields could lead to a twofold symmetry of the in-plane H_c if vortices move freely, the observed results in EuO_x/KTO are independent of the current direction (fig. S10), which would rule out this mechanism for an anisotropic Fermi surface. More recently, twofold H_c modulations have been ascribed to anisotropic spin susceptibilities that result from 3D spin textures of the Fermi surface due to broken mirror symmetries and the interplay of parity with SOC near band-inversion points in reciprocal space (*55*–*57*).

Downloaded from https://www.science.org at Florida State University on September 02, 2026

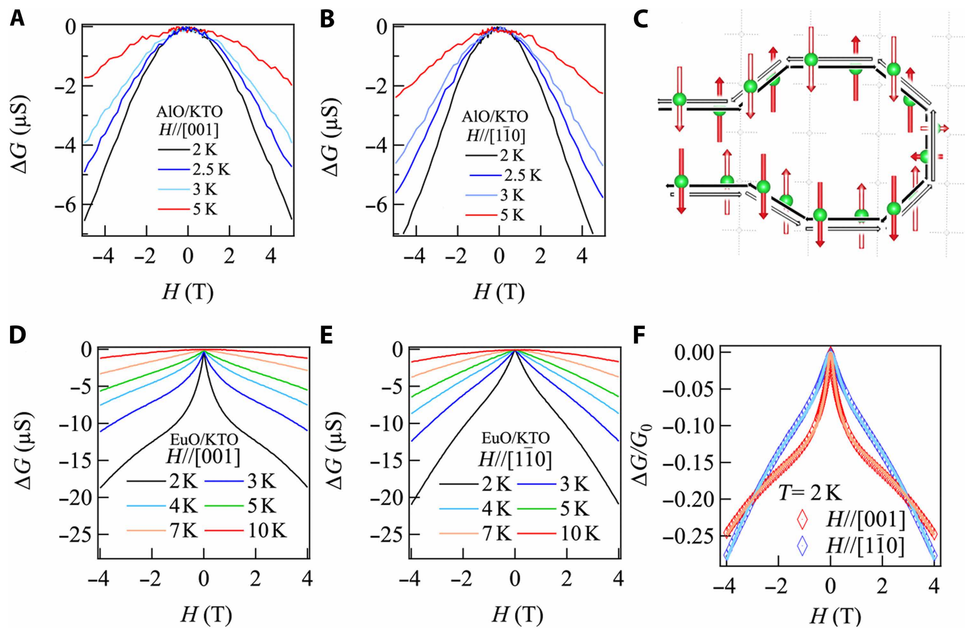

Fig. 5. Anisotropic WAL of KTO (110). Field dependence of the magnetoconductance at different temperatures for AlO_x/KTO for an in-plane magnetic field applied (**A**) along the [001] direction and (**B**) along the [1$\bar{1}$0] direction. (**D** and **E**) Same as (A) and (B), but for EuO_x/KTO. (**C**) Schematic of the destructive interference for an electron scattering in time-reversed closed loop paths in KTO (110) with spins (shown by solid and hollow red arrows) locked along the [001] axis. (**F**) Weak antilocalization (WAL) fits to the magnetoconductance of EuO_x/KTO at 2 K for both in-plane field directions as described in the text.

However, corroborating experimental evidence for these spin textures is not well established.

In summary, we find evidence for an in-plane uniaxial spin texture in KTO (110) 2DEGs. The texture is hidden in AlO_x/KTO due to a strongly reduced *g*-factor of the Ta conduction electrons, but, for EuO_x/KTO, the presence of an exchange field from the Eu ions "lights up" the Ta-5d spin texture and allows us to see its consequences for both the critical field in the superconducting state as well the low-temperature normal state magnetoconductance. The anisotropic response in the superconducting state is consistent with the uniaxial half-Rashba ($\mathbf{k}_y\hat{\sigma}_x$) spin texture that occurs in the d_{yz}/d_{xz} bands. Our results also imply that carriers in d_{xy} bands, which lack such a uniaxial spin texture, do not contribute. These carriers also do not participate in the WAL-like response to in-plane fields. The unique in-plane half-Rashba like nature of the spin texture intrinsic to KTO (110) 2DEGs may have consequences for spin-orbitronics (*58*) as the Rashba-Edelstein length should be highly anisotropic in plane. In the context of unconventional superconductivity, the triplet component of the Cooper pairs that can be admixed due to inversion symmetry breaking (*5*) should exhibit the same in-plane uniaxial anisotropy as we find here. Our results lend insight into the nature of exchange interactions at the EuO/KTO interface and the role of Eu interdiffusion in KTO. In addition to probing spin textures, magnetic proximity effects also offer a path to control superconductivity in spin-textured materials.

MATERIALS AND METHODS

Sample fabrication

AlO_x/KTO samples were prepared by depositing pure Al on a single crystal KTO (110) substrate in a temperature range from 500° to 600°C under 10^{-9}-mbar pressure in a molecular beam epitaxy chamber. The EuO_x/KTO sample was prepared by depositing pure Eu on a single crystal KTO (110) substrate at a temperature of 500°C under 10^{-8}-mbar oxygen pressure in a molecular beam epitaxy chamber (*17*, *19*). A 10-nm Ge capping layer was deposited on all samples as a protecting layer. Hall bar patterns were prepared using by means of a maskless laser photolithography system (MLA 150, Heidelberg; photoresist AR-P 5350, Allresist EN). Pattern transfer from the photoresist onto the samples was realized using liq-N_2 cooled Ar-based ion-beam etching.

Transport measurements

The low-temperature transport measurements down to 50 mK were carried out in a Bluefors dilution fridge equipped with a 9-1-1 vector magnet. The out-of-plane magnetic field component for a given in-plane magnetic field was zeroed out by searching for minima in the magnetoresistance while sweeping the out-of-plane field about zero.

The 23-mK field dependence of the resistance measurement in parallel fields was carried out in an 18-T cryogenic station at the National High Magnetic Field Laboratory, with the sample mounted on a rotator. The zeroing out of the out-of-plane component was achieved by searching for minima in the angular dependence of the resistance while rotating the sample. The magnetoconductance measurements at higher temperature were carried out through a rotator in a 14 T Physical Properties Measurement System from Quantum Design.

Statement regarding error bars

In Figs. 1 to 3 and 5, the uncertainty/error in the plotted data points is smaller than the symbols used to represent the data. For Fig. 4, the error bars for the diffusion lengths of the Eu^{2+} and Eu^{3+} in KTO are

Downloaded from https://www.science.org at Florida State University on September 02, 2026

estimated from the scatter in the intensity of the spectral signatures with position.

Supplementary Materials

This PDF file includes:
Supplementary Text S1 to S14
Figs. S1 to S18
Tables S1 to S3
References

REFERENCES

1. G. Bihlmayer, P. Noël, D. V. Vyalikh, E. V. Chulkov, A. Manchon, Rashba-like physics in condensed matter. *Nat. Rev. Phys.* **4**, 642–659 (2022).
2. S. Picozzi, Spin–orbit coupling in quantum materials: Emergent phenomena, their modelling and examples from two-dimensional magnets. *Riv. Nuovo Cimento.* **47**, 609–652 (2024).
3. Y. A. Bychkov, E. I. Rashba, Properties of a 2D electron-gas with lifted spectral degeneracy. *JETP Lett.* **39**, 78–81 (1984).
4. M. Smidman, M. B. Salamon, H. Q. Yuan, D. F. Agterberg, Superconductivity and spin–orbit coupling in non-centrosymmetric materials: A review. *Rep. Prog. Phys.* **80**, 036501 (2017).
5. L. P. Gor'kov, E. I. Rashba, Superconducting 2D system with lifted spin degeneracy: Mixed singlet-triplet state. *Phys. Rev. Lett.* **87**, 037004 (2001).
6. J. M. Lu, O. Zheliuk, I. Leermakers, N. F. Q. Yuan, U. Zeitler, K. T. Law, J. T. Ye, Evidence for two-dimensional Ising superconductivity in gated MoS_2. *Science* **350**, 1353–1357 (2015).
7. Y. Saito, Y. Nakamura, M. S. Bahramy, Y. Kohama, J. Ye, Y. Kasahara, Y. Nakagawa, M. Onga, M. Tokunaga, T. Nojima, Y. Yanase, Y. Iwasa, Superconductivity protected by spin–valley locking in ion-gated MoS_2. *Nat. Phys.* **12**, 144–149 (2016).
8. J. Falson, Y. Xu, M. Liao, Y. Zang, K. Zhu, C. Wang, Z. Zhang, H. Liu, W. Duan, K. He, H. Liu, J. H. Smet, D. Zhang, Q.-K. Xue, Type-II Ising pairing in few-layer stanene. *Science* **367**, 1454–1457 (2020).
9. B. T. Zhou, N. F. Q. Yuan, H. L. Jiang, K. T. Law, Ising superconductivity and Majorana fermions in transition-metal dichalcogenides. *Phys. Rev. B* **93**, 180501 (2016).
10. K. Matano, M. Kriener, K. Segawa, Y. Ando, G. Q. Zheng, Spin-rotation symmetry breaking in the superconducting state of $Cu_xBi_2Se_3$. *Nat. Phys.* **12**, 852–854 (2016).
11. A. Hamill, B. Heischmidt, E. Sohn, D. Shaffer, K. T. Tsai, X. Zhang, X. X. Xi, A. Suslov, H. Berger, L. Forró, F. J. Burnell, J. Shan, K. F. Mak, R. M. Fernandes, K. Wang, V. S. Pribiag, Two-fold symmetric superconductivity in few-layer $NbSe_2$. *Nat. Phys.* **17**, 949–954 (2021).
12. A. Johansson, J. Henk, I. Mertig, Theoretical aspects of the Edelstein effect for anisotropic two-dimensional electron gas and topological insulators. *Phys. Rev. B* **93**, 195440 (2016).
13. S. M. Frolov, M. J. Manfra, J. D. Sau, Topological superconductivity in hybrid devices. *Nat. Phys.* **16**, 718–724 (2020).
14. M. M. Desjardins, L. C. Contamin, M. R. Delbecq, M. C. Dartiailh, L. E. Bruhat, T. Cubaynes, J. J. Viennot, F. Mallet, S. Rohart, A. Thiaville, A. Cottet, T. Kontos, Synthetic spin-orbit interaction for Majorana devices. *Nat. Mater.* **18**, 1060–1064 (2019).
15. J. Linder, J. W. A. Robinson, Superconducting spintronics. *Nat. Phys.* **11**, 307–315 (2015).
16. M. Amundsen, J. Linder, J. W. A. Robinson, I. Zutic, N. Banerjee, Spin-orbit effects in superconducting hybrid structures. *Rev. Mod. Phys.* **96**, 021003 (2024).
17. C. Liu, X. Yan, D. Jin, Y. Ma, H.-W. Hsiao, Y. Lin, T. M. Bretz-Sullivan, X. Zhou, J. Pearson, B. Fisher, J. S. Jiang, W. Han, J.-M. Zuo, J. Wen, D. D. Fong, J. Sun, H. Zhou, A. Bhattacharya, Two-dimensional superconductivity and anisotropic transport at $KTaO_3$ (111) interfaces. *Science* **371**, 716–721 (2021).
18. Z. Chen, Z. R. Liu, Y. Q. Sun, X. X. Chen, Y. Liu, H. Zhang, H. K. Li, M. Zhang, S. Y. Hong, T. S. Ren, C. Zhang, H. Tian, Y. Zhou, J. R. Sun, Y. W. Xie, Two-dimensional superconductivity at the $LaAlO_3/KTaO_3$ (110) heterointerface. *Phys. Rev. Lett.* **126**, 026802 (2021).
19. C. Liu, X. Zhou, D. Hong, B. Fisher, H. Zheng, J. Pearson, J. S. Jiang, D. Jin, M. R. Norman, A. Bhattacharya, Tunable superconductivity and its origin at $KTaO_3$ interfaces. *Nat. Commun.* **14**, 951 (2023).
20. E. A. Martínez, J. Dai, M. Tallarida, N. M. Nemes, F. Y. Bruno, Anisotropic electronic structure of the 2D electron gas at the $AlO_x/KTaO_3$(110) interface. *Adv. Electron. Mater.* **9**, 2300267 (2023).
21. P. W. Krantz, A. Tyner, P. Goswami, V. Chandrasekhar, Nonlinear hall effect in $KTaO_3$ two-dimensional electron gases. arXiv:2411.09161 (2024).
22. S. J. Poage, X. S. Gao, M. Baksi, S. Salmani-Rezaie, D. A. Muller, D. P. Kumah, C. N. Lau, J. Lorenzana, M. N. Gastiasoro, K. Ahadi, Violation of the Pauli limit at KTaO (110) interfaces. *Phys. Rev. B* **111**, 214506 (2025).
23. F. Y. Bruno, S. M. Walker, S. Riccò, A. de la Torre, Z. M. Wang, A. Tamai, T. K. Kim, M. Hoesch, M. S. Bahramy, F. Baumberger, Band structure and spin-orbital texture of the (111)-$KTaO_3$ 2D electron gas. *Adv. Electron Mater.* **5**, 1800860 (2019).
24. S. Varotto, A. Johansson, B. Göbel, L. M. Vicente-Arche, S. Mallik, J. Bréhin, R. Salazar, F. Bertran, P. Le Fèvre, N. Bergeal, J. Rault, I. Mertig, M. Bibes, Direct visualization of Rashba-split bands and spin/orbital-charge interconversion at $KTaO_3$ interfaces. *Nat. Commun.* **13**, 6165 (2022).
25. S. Sugano, Y. Tanabe, H. Kamimura, *Multiplets of Transition-Metal Ions in Crystals* (Elsevier Science, 1970).
26. A. H. Al-Tawhid, S. J. Poage, S. Salmani-Rezaie, A. Gonzalez, S. Chikara, D. A. Muller, D. Kumah, M. N. Gastiasoro, J. Lorenzana, K. Ahadi, Enhanced critical field of superconductivity at an oxide interface. *Nano Lett.* **23**, 6944–6950 (2023).
27. G. Singh, A. Jouan, G. Herranz, M. Scigaj, F. Sánchez, L. Benfatto, S. Caprara, M. Grilli, G. Saiz, F. Couëdo, C. Feuillet-Palma, J. Lesueur, N. Bergeal, Gap suppression at a Lifshitz transition in a multi-condensate superconductor. *Nat. Mater.* **18**, 948–954 (2019).
28. A. Annadi, Q. Zhang, X. Renshaw Wang, N. Tuzla, K. Gopinadhan, W. M. Lü, A. Roy Barman, Z. Q. Liu, A. Srivastava, S. Saha, Y. L. Zhao, S. W. Zeng, S. Dhar, E. Olsson, B. Gu, S. Yunoki, S. Maekawa, H. Hilgenkamp, T. Venkatesan, Ariando, Anisotropic two-dimensional electron gas at the $LaAlO_3/SrTiO_3$ (110) interface. *Nat.Commun.* **4**, 1838 (2013).
29. Z. Wang, Z. Zhong, X. Hao, S. Gerhold, B. Stöger, M. Schmid, J. Sánchez-Barriga, A. Varykhalov, C. Franchini, K. Held, U. Diebold, Anisotropic two-dimensional electron gas at $SrTiO_3$ (110). *Proc. Natl. Acad. Sci. U.S.A.* **111**, 3933–3937 (2014).
30. P. Moetakef, J. R. Williams, D. G. Ouellette, A. P. Kajdos, D. Goldhaber-Gordon, S. J. Allen, S. Stemmer, Carrier-controlled ferromagnetism in $SrTiO_3$. *Phys. Rev. X* **2**, 021014 (2012).
31. D. A. Dikin, M. Mehta, C. W. Bark, C. M. Folkman, C. B. Eom, V. Chandrasekhar, Coexistence of superconductivity and ferromagnetism in two dimensions. *Phys. Rev. Lett.* **107**, 056802 (2011).
32. F. Wen, Y. Cao, X. Liu, B. Pal, S. Middey, M. Kareev, J. Chakhalian, Evolution of ferromagnetism in two-dimensional electron gas of $LaTiO_3/SrTiO_3$. *Appl. Phys. Lett.* **112**, 122405 (2018).
33. P. W. Krantz, A. Tyner, P. Goswami, V. Chandrasekhar, Intrinsic magnetism in $KTaO_3$ heterostructures. *Appl. Phys. Lett.* **124**, 093102 (2024).
34. X. Hua, Z. Zeng, F. Meng, H. Yao, Z. Huang, X. Long, Z. Li, Y. Wang, Z. Wang, T. Wu, Z. Weng, Y. Wang, Z. Liu, Z. Xiang, X. Chen, Superconducting stripes induced by ferromagnetic proximity in an oxide heterostructure. *Nat. Phys.* **20**, 957–963 (2024).
35. K. Maki, T. Tsuneto, Pauli paramagnetism and superconducting state. *Prog. Theor. Phys.* **31**, 945–956 (1964).
36. Z. Zhang, W. Jiang, T. Shao, Y. Qiao, X. Chen, Q. Zhao, M. Chen, R. Dou, C. Xiong, J. Nie, A spin–orbit scattering–enhanced high upper critical field at the $LaAlO_3/KTaO_3$(111) superconducting interface. *New J. Phys.* **25**, 023023 (2023).
37. E. G. Arnault, A. H. Al-Tawhid, S. Salmani-Rezaie, D. A. Muller, D. P. Kumah, M. S. Bahramy, G. Finkelstein, K. Ahadi, Anisotropic superconductivity at $KTaO_3$ (111) interfaces. *Sci. Adv.* **9**, eadf1414 (2023).
38. M. Tinkham, *Introduction to Superconductivity* (Dover Publications, 2004).
39. N. R. Werthamer, E. Helfand, P. C. Hohenberg, Temperature and purity dependence of the superconducting critical field, H_{c2}. III. Electron spin and spin-orbit effects. *Phys. Rev.* **147**, 295–302 (1966).
40. O. Fischer, M. Decroux, S. Roth, R. Chevrel, M. Sergent, Compensation of the paramagnetic effect on H_{c2} by magnetic moments: 700 kG superconductors. *J. Phys. C. Solid Stat. Phys.* **8**, L474–L477 (1975).
41. H. Xu, H. Li, N. Gauquelin, X. Chen, W.-F. Wu, Y. Zhao, L. Si, D. Tian, L. Li, Y. Gan, S. Qi, M. Li, F. Hu, J. Sun, D. Jannis, P. Yu, G. Chen, Z. Zhong, M. Radovic, J. Verbeeck, Y. Chen, B. Shen, Giant tunability of rashba splitting at cation-exchanged polar oxide interfaces by selective orbital hybridization. *Adv. Mater.* **36**, e2313297 (2024).
42. B. Lama, E. Y. Tsymbal, T. R. Paudel, Effects of intermixing and oxygen vacancies on a two-dimensional electron gas at the polar $TbScO_3/KTaO_3$ (001) interface. *Phys. Rev. Mater.* **7**, 026201 (2023).
43. R. A. Klemm, A. Luther, M. R. Beasley, Theory of upper critical-field in layered superconductors. *Phys. Rev. B* **12**, 877–891 (1975).
44. O. H. Fischer, Properties of high-field superconductors containing localized magnetic moments. *Helv. Phys. Acta* **45**, 331–397 (1972).
45. Y. Gan, F. Yang, L. Kong, X. Chen, H. Xu, J. Zhao, G. Li, Y. Zhao, L. Yan, Z. Zhong, Y. Chen, H. Ding, Light-induced giant rashba spin–orbit coupling at superconducting $KTaO_3$ (110) heterointerfaces. *Adv. Mater.* **35**, e2300582 (2023).
46. A. H. Al-Tawhid, J. Kanter, M. Hatefipour, D. P. Kumah, J. Shabani, K. Ahadi, Superconductivity and weak anti-localization at $KTaO_3$ (111) interfaces. *J. Electron. Mater.* **51**, 6305–6309 (2022).
47. X. Hua, F. Meng, Z. Huang, Z. Li, S. Wang, B. Ge, Z. Xiang, X. Chen, Tunable two-dimensional superconductivity and spin-orbit coupling at the $EuO/KTaO_3$(110) interface. *NPJ Quant. Mater.* **7**, 97 (2022).
48. X. Cai, Y. Ayino, J. Yue, P. Xu, B. Jalan, V. S. Pribiag, Disentangling spin-orbit coupling and local magnetism in a quasi-two-dimensional electron system. *Phys. Rev. B* **100**, 081402 (2019).
49. S. Maekawa, H. Fukuyama, Magnetoresistance in two-dimensional disordered systems: Effects of zeeman splitting and spin-orbit scattering. *J. Physical Soc. Japan* **50**, 2516–2524 (1981).

Downloaded from https://www.science.org at Florida State University on September 02, 2026

50. F. F. Balakirev, T. Kong, M. Jaime, R. D. McDonald, C. H. Mielke, A. Gurevich, P. C. Canfield, S. L. Bud'ko, Anisotropy reversal of the upper critical field at low temperatures and spin-locked superconductivity in $K_2Cr_3As_3$. *Phys. Rev. B* **91**, 220505 (2015).
51. J. K. Bao, J. Y. Liu, C. W. Ma, Z. H. Meng, Z. T. Tang, Y. L. Sun, H. F. Zhai, H. Jiang, H. Bai, C. M. Feng, Z. A. Xu, G. H. Cao, Superconductivity in quasi-one-dimensional $K_2Cr_3As_3$ with significant electron correlations. *Phys. Rev. X* **5**, 011013 (2015).
52. H. K. Zuo, J. K. Bao, Y. Liu, J. H. Wang, Z. Jin, Z. C. Xia, L. Li, Z. Xu, J. Kang, Z. W. Zhu, G. H. Cao, Temperature and angular dependence of the upper critical field in $K_2Cr_3As_3$. *Phys. Rev. B* **95**, 014502 (2017).
53. J. Yang, J. Luo, C. Yi, Y. Shi, Y. Zhou, G. Q. Zheng, Spin-triplet superconductivity in $K_2Cr_3As_3$. *Sci. Adv.* **7**, eabl4432 (2021).
54. I. Silber, S. Mathimalar, I. Mangel, A. K. Nayak, O. Green, N. Avraham, H. Beidenkopf, I. Feldman, A. Kanigel, A. Klein, M. Goldstein, A. Banerjee, E. Sela, Y. Dagan, Two-component nematic superconductivity in 4Hb-TaS_2. *Nat. Commun.* **15**, 824 (2024).
55. Y. M. Xie, B. T. Zhou, K. T. Law, Spin-orbit-parity-coupled superconductivity in topological monolayer WTe_2. *Phys. Rev. Lett.* **125**, 107001 (2020).
56. J. Cui, P. Li, J. Zhou, W. Y. He, X. Huang, J. Yi, J. Fan, Z. Ji, X. Jing, F. Qu, Z. G. Cheng, C. Yang, L. Lu, K. Suenaga, J. Liu, K. T. Law, J. Lin, Z. Liu, G. Liu, Transport evidence of asymmetric spin-orbit coupling in few-layer superconducting $1T_d$-$MoTe_2$. *Nat. Commun.* **10**, 2044 (2019).
57. E. Z. Zhang, Y. M. Xie, Y. Q. Fang, J. L. Zhang, X. Xu, Y. C. Zou, P. L. Leng, X. J. Gao, Y. Zhang, L. F. Ai, Y. D. Zhang, Z. H. Jia, S. S. Liu, J. Y. Yan, W. Zhao, S. J. Haigh, X. F. Kou, J. S. Yang, F. Q. Huang, K. T. Law, F. X. Xiu, S. M. Dong, Spin-orbit-parity coupled superconductivity in atomically thin 2M-WS_2. *Nat. Phys.* **19**, 106–113 (2023).
58. P. He, S. M. Walker, S. S. L. Zhang, F. Y. Bruno, M. S. Bahramy, J. M. Lee, R. Ramaswamy, K. Cai, O. Heinonen, G. Vignale, F. Baumberger, H. Yang, Observation of out-of-plane spin texture in a $SrTiO_3$ (111) two-dimensional electron gas. *Phys. Rev. Lett.* **120**, 266802 (2018).
59. H. Zhang, Y. Yun, X. Zhang, H. Zhang, Y. Ma, X. Yan, F. Wang, G. Li, R. Li, T. Khan, Y. Chen, W. Liu, F. Hu, B. Liu, B. Shen, W. Han, J. Sun, High-mobility spin-polarized two-dimensional electron gases at EuO/$KTaO_3$ interfaces. *Phys. Rev. Lett.* **121**, 116803 (2018).
60. T. Yamasaki, K. Ueno, A. Tsukazaki, T. Fukumura, M. Kawasaki, Observation of anomalous Hall effect in EuO epitaxial thin films grown by a pulse laser deposition. *Appl. Phys. Lett.* **98**, 082116 (2011).
61. D. Xiao, W. Zhu, Y. Ran, N. Nagaosa, S. Okamoto, Interface engineering of quantum Hall effects in digital transition metal oxide heterostructures. *Nat. Commun.* **2**, 596 (2011).
62. A. Jain, S. P. Ong, G. Hautier, W. Chen, W. D. Richards, S. Dacek, S. Cholia, D. Gunter, D. Skinner, G. Ceder, K. A. Persson, Commentary: The materials project: A materials genome approach to accelerating materials innovation. *APL Materials* **1**, 011002 (2013).
63. W. T. Vetterling, S. A. Teukolsky, W. H. Press, B. P. Flannery, *Numerical Recipes* (Cambridge Univ. Press, ed. 2, 1992).
64. V. Jaccarino, M. Peter, Ultra-high-field superconductivity. *Phys. Rev. Lett.* **9**, 290–292 (1962).

Acknowledgments

Funding: All research presented here is supported by the Materials Science and Engineering Division, Office of Basic Energy Sciences, US Department of Energy. Work performed at the Center for Nanoscale Materials, a US Department of Energy Office of Science User Facility, was supported by the US Department of Energy, Office of Basic Energy Sciences, under contract no. DE-AC02-06CH11357. C.L. acknowledges partial financial support from the College of Arts and Sciences, University at Buffalo, SUNY. The National High Magnetic Field Laboratory is supported by the National Science Foundation through NSF/DMR-1644779 and NSF/DMR-2128556 and the State of Florida. We thank I. Martin for discussions. **Author contributions:** Synthesis of samples was carried out by J.Y. and C.L. with assistance from A.B. and J.P. All low-temperature magneto-transport and magnetization measurements were carried out by J.Y. and C.L. with assistance from U.W., A.S., J.S.J., X.Z., and D.J. The theoretical analysis presented here was carried out by M.R.N. along with J.Y. and A.B. The paper was written by J.Y., M.R.N., and A.B., and all authors contributed to discussions regarding the paper. **Competing interests:** The authors declare that they have no competing interests. **Data, code, and materials availability:** All data and code needed to evaluate and reproduce the results in the paper are present in the paper and/or the Supplementary Materials. All data for figures in the manuscript are available via the Harvard Dataverse at the following link: https://doi.org/10.7910/DVN/VYIOWB. This study did not generate new materials.

Submitted 3 August 2025
Accepted 2 April 2026
Published 8 May 2026
10.1126/sciadv.aeb1601

Downloaded from https://www.science.org at Florida State University on September 02, 2026

Science Advances

Uniaxial spin texture in a superconducting electron gas revealed by exchange interactions

Junyi Yang, Changjiang Liu, Xianjing Zhou, Hanyu Hou, Kaijun Yin, Jianguo Wen, John Pearson, Alexey Suslov, Dafei Jin, Jidong S. Jiang, Ulrich Welp, Jian-Min Zuo, Michael R. Norman, and Anand Bhattacharya

Sci. Adv. **12** (19), eaeb1601. DOI: 10.1126/sciadv.aeb1601

View the article online
https://www.science.org/doi/10.1126/sciadv.aeb1601
Permissions
https://www.science.org/help/reprints-and-permissions

Downloaded from https://www.science.org at Florida State University on September 02, 2026

Use of this article is subject to the Terms of service

Science Advances (ISSN 2375-2548) is published by the American Association for the Advancement of Science. 1200 New York Avenue NW, Washington, DC 20005. The title *Science Advances* is a registered trademark of AAAS.

Copyright © 2026 The Authors, some rights reserved; exclusive licensee American Association for the Advancement of Science. No claim to original U.S. Government Works. Distributed under a Creative Commons Attribution License 4.0 (CC BY).